Noninvasive Imaging of CD4$^+$ T Cells in Humanized Mice

Veronica L. Nagle[1,2], Charli Ann J. Hertz[2], Kelly E. Henry[3], Maya S. Graham[4,5], Carl Campos[2], Nagavarakishore Pillarsetty[3,6,7], Andrea Schietinger[8], Ingo K. Mellinghoff[1,2,4,5,9], and Jason S. Lewis[1,3,6,7,9]

ABSTRACT

Antibody-based PET (immunoPET) with radiotracers that recognize specific cells of the immune system provides an opportunity to monitor immune cell trafficking at the organismal scale. We previously reported the visualization of human CD8$^+$ T cells, including CD8$^+$ tumor-infiltrating lymphocytes (TIL), in mice using a humanized CD8-targeted minibody. Given the important role of CD4$^+$ T cells in adaptive immune responses of health and disease including infections, tumors, and autoimmunity, we explored immunoPET using an anti-human-CD4 minibody. We assessed the ability of [^{64}Cu]Cu-NOTA-IAB41 to bind to various CD4$^+$ T-cell subsets *in vitro*. We also determined the effect of the CD4-targeted minibody on CD4$^+$ T-cell abundance, proliferation, and activation state *in vitro*. We subsequently evaluated the ability of the radiotracer to visualize CD4$^+$ T cells in T-cell rich organs and orthotopic brain tumors *in vivo*. For the latter, we injected the [^{64}Cu]Cu-NOTA-IAB41 radiotracer into humanized mice that harbored intracranial patient-derived glioblastoma (GBM) xenografts and performed *in vivo* PET, *ex vivo* autoradiography, and anti-CD4 IHC on serial brain sections. [^{64}Cu]Cu-NOTA-IAB41 specifically detects human CD4$^+$ T cells without impacting their abundance, proliferation, and activation. In humanized mice, [^{64}Cu]Cu-NOTA-IAB41 can visualize various peripheral tissues in addition to orthotopically implanted GBM tumors. [^{64}Cu]Cu-NOTA-IAB41 is able to visualize human CD4$^+$ T cells in humanized mice and can provide noninvasive quantification of CD4$^+$ T-cell distribution on the organismal scale.

Introduction

Antibodies targeting immune checkpoints induce durable tumor regression and prolonged survival in subsets of patients with primary and brain-resident metastatic melanoma and non–small cell lung cancer (1–3). However, many patients do not respond. Further development of effective immunotherapeutic candidates will require a deeper understanding of the effect of these drugs on immune cell activation and *in vivo* immune cell localization (4). This is particularly relevant for CD8$^+$ and CD4$^+$ T lymphocytes, which migrate between the tumor and lymphatic organs to develop effective antitumor immunity (5).

Compared with CD8$^+$ T cells, the contribution of specific CD4$^+$ T-cell subsets toward the antitumor immune response is less well characterized (6). Studies in mouse cancer models demonstrated that CD4$^+$ T cells were necessary to maintain a CD8$^+$ antitumor immune response (7, 8). Further, clinical vaccine studies suggest that CD4$^+$ T cells can mediate the development and maintenance of antitumor immunity (9, 10). CD4$^+$ T cells are polyfunctional cells which differentiate into distinct subtypes with different implications for antitumor immunity. Upon activation naïve CD4$^+$ T cells can differentiate into conventional helper T-cell (T_H) subtypes or nonconventional regulatory T cells (T_{regs}). Conventional CD4$^+$ T cells drive antitumor CD8$^+$ T-cell effector function, provide CD40 ligand signaling to induce B-cell antibody production, and are capable of directly inducing tumor cell lysis (11). Collectively, T_{regs} are a subset distinct from the conventional CD4$^+$ effector lineage and are known to mediate tumor-associated immunosuppression (12).

The need to develop noninvasive diagnostic platforms to monitor immune cell distribution is particularly urgent for patients with glioblastoma (GBM), the most common primary malignant brain tumor in adults. Antibodies targeting the PD-1 immune checkpoint in malignant glioma have failed to show clinical activity in phase III trials despite evidence for T-cell activation in GBM tumor biopsies (13, 14). There is growing evidence implicating CD4$^+$ T cells in the antitumor response to PD-1/PD-L1 immune checkpoint blockade. For example, CD4$^+$ T cells express PD-1 in patients with lung cancer and the depletion of CD4$^+$ T cells in an orthotopic mouse model of lung cancer reduced anti-PD1 therapeutic efficacy (15). Further, CD4$^+$ T cells were required for anti-PD-1 response in mouse models of melanoma (16). Determination of CD4$^+$ T-cell abundance in the GBM tumor microenvironment and of CD4$^+$ T-cell distribution on the organismal scale may hence provide insight into immunotherapeutic resistance in patients with GBM. However, repeated access to tumor tissue samples is difficult and the tools do not exist to measure immune cell densities in brain tumors throughout treatment course. There is a need for noninvasive immune cell monitoring tools to enable a thorough and rigorous study of immunotherapeutic resistance and response in GBM and other brain tumors. Noninvasive visualization of CD4$^+$ T cells circumvents invasive biopsy and enables the study of CD4$^+$ T-cell kinetics in brain tumors over time.

[1]Department of Pharmacology, Weill Cornell Medical College, New York, New York. [2]Human Oncology and Pathogenesis Program, Memorial Sloan Kettering Cancer Center, New York, New York. [3]Department of Radiology, Memorial Sloan Kettering Cancer Center, New York, New York. [4]Brain Tumor Center, Memorial Sloan Kettering Cancer Center, New York, New York. [5]Department of Neurology, Memorial Sloan Kettering Cancer Center, New York, New York. [6]Department of Radiology, Weill Cornell Medical College, New York, New York. [7]Radiochemistry and Molecular Imaging Probes Core, Memorial Sloan Kettering Cancer Center, New York, New York. [8]Immunology Program, Memorial Sloan Kettering Cancer Center, New York, New York. [9]Molecular Pharmacology Program, Memorial Sloan Kettering Cancer Center, New York, New York.

Note: Supplementary data for this article are available at Molecular Cancer Therapeutics Online (http://mct.aacrjournals.org/).

Corresponding Authors: Jason S. Lewis, Radiology and Molecular Pharmacology, Memorial Sloan Kettering Cancer Center, 1275 York Avenue, New York, NY 10065. E-mail: lewisj2@mskcc.org; Ingo K. Mellinghoff, Neurology and Human Oncogenesis and Pathology Program, Memorial Sloan Kettering Cancer Center, E-mail: mellingi@mskcc.org

Mol Cancer Ther 2022;21:658–66

doi: 10.1158/1535-7163.MCT-21-0888

To address this need, we utilized an anti-human-CD4 immunoPET tracer. The ideal CD4 immunoPET reagent for patients with brain tumor would enable high target-to-background ratio, rapid imaging turn around, and would not display unwanted biological activities. Prior to our work, a mouse-specific cys-diabody-based immunoPET tracer noninvasively detected mouse $CD4^+$ T cells in mouse models of colitis (17) and hematopoietic stem cell expansion (18). However, the cys-diabody induced the depletion of $CD4^+$ T cells, which may limit the clinical applicability of this radiotracer (19). Another mouse-specific CD4-targeted F(ab)'2 immunoPET tracer detected mouse $CD4^+$ T cells following anti-PD-1 checkpoint blockade in syngeneic skin, mast cell, colon, kidney, and breast cancer models at 24 hours after radiotracer injection (20). Both the CD4-targeted cys-diabody and F(ab)'2 radiotracers are mouse specific, limiting clinical translation. To address this gap and develop a radiotracer for use in patients, we evaluated a humanized CD4-targeted immunoPET tracer to detect human $CD4^+$ T cells. We opted to evaluate a human-specific anti-CD4 minibody as the serum half-life of a minibody enables high tumor-to-background ratios within 24 hours of radiotracer injection and the truncated Fc region renders the Fc region of the minibody biologically inert. In summary, a human CD4-targeted minibody-based approach satisfies the criteria for optimal immunoPET imaging.

Several prior studies have used humanized immune system (HIS) mouse models to evaluate imaging of human immune cells using novel PET tracers, but none of these studies explored imaging of brain tumors (21–24). Our group recently reported HIS mouse models of GBM to evaluate the capacity of a human CD8-targeted minibody to detect tumor-infiltrating lymphocytes (TIL) in the brain tumor microenvironment (TME; ref. 25). In this study, we seek to expand immunoPET to other immune cell types and, specifically, to evaluate the ability of a CD4-targeted minibody to detect $CD4^+$ T cells in peripheral organs as well as brain TILs.

Materials and Methods

Radiolabeling and synthesis of [^{64}Cu]Cu-NOTA-IAB41

The radiotracer synthesis and radiolabeling approach is depicted in **Fig. 1A**. An 80-fold excess of 2-S-(4-Isothiocyanatobenzyl)-1,4,7-triazacyclononane-1,4,7-triacetic acid (p-SCN-Bn-NOTA; Macrocyclics, catalog no. B-605) was incubated with the humanized anti-CD4 minibody (IAB41, ImaginAb) in metal-free PBS at pH 8.8 for 4 hours at 4°C. NOTA-IAB41 was subsequently purified using Zeba spin column (Thermo Fisher Scientific, Molecular Weight Cut Off 7 kDa). [^{64}Cu]$CuCl_2$ was obtained from the University of Washington St. Louis. NOTA-IAB41 (0.2 mg) was diluted to a total reaction volume of 100 μL metal-free 250 mmol/L ammonium acetate and incubated with 74 MBq (2 mCi) of ^{64}Cu at 42°C for 30 minutes at pH 5.5 and purified using Zeba spin column into metal-free PBS. Radiochemical purity and stability in human serum were assessed using thin later chromatography using a 50 mmol/L EDTA (pH 5) eluent. Specific activity of [^{64}Cu]Cu-NOTA-IAB41 ranged between 296 and 444 MBq/mg (8–12 mCi/mg).

Animal models

All animal experiments were performed in accordance with and with approval of the Institutional Animal Care and Use Committee (IACUC) at Memorial Sloan Kettering Cancer Center (MSKCC). To generate humanized immune system (HIS) mice, 10^7 HLA-typed peripheral blood mononuclear cells (PBMC) from individual donors (Stem Cell Technologies, catalog no. 70025) were injected into the tail vein of a 6- to 8-week-old female CIEA NOG mice (Taconic, RRID; ISMR_TAC:NOG). GBM patient-derived xenografts (PDX) 160721–1 and 160615–1 were derived from recurrent WHO grade IV GBMs as described previously (25). GBM PDX-bearing HIS mice were generated using methods described previously (25). No mycoplasma testing was performed. All experiments were performed on PDX passages 4 to

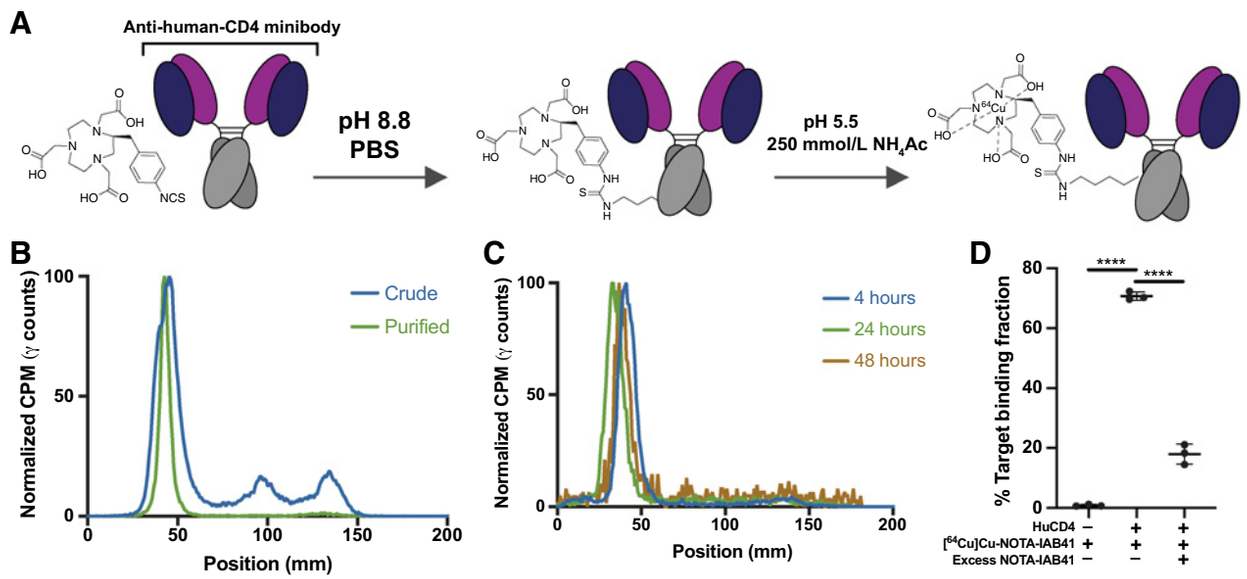

Figure 1.

[^{64}Cu]Cu-NOTA-IAB41 synthesis and radiolabeling. **A,** Synthesis and radiolabeling workflow of [^{64}Cu]Cu-NOTA-IAB41 (25). **B,** Radiolabeling and purification of [^{64}Cu]Cu-NOTA-IAB41 quantified by iTLC. **C,** Stability of [^{64}Cu]Cu-NOTA-IAB41 in human serum quantified by iTLC. **D,** Recombinant human CD4 *in vitro* bead-based immunoreactivity assay. Excess NOTA-IAB41 = 100-fold excess. For all panels error bars are the SD (****, $P \leq 0.0001$).

5. Three weeks following intracranial tumor implantation, mice were injected with PBMCs as described above.

Protein binding assay

The protein binding assay was conducted using previously described methods (26) and used recombinant human CD4 protein (Sino Biological, catalog no. 10400-H08H-B-20).

Flow cytometry

For each flow cytometry experiment, pooled cells from all samples were used to generate fluorescence minus one (FMO) and unstained controls. Ultracomp eBeads (Thermo Fisher Scientific, catalog no. 01–2222–41) were stained to generate single color controls. Analysis was performed using FlowJo (Version 10, RRID:SCR_008520). Flow cytometry was performed on the BD LSRFortessa.

PBMC flow cytometry

Human PBMCs were stained with BV421-CD4 (BioLegend, OKT4, catalog no. 304222, RRID: AB_2562134), PE/Cy7-CD25 (BioLegend, M-A251, catalog no. 356108, RRID: AB_2561975), PE-CD45RA (BioLegend, HI100, catalog no. 304108, RRID: AB_314412), PerCP/Cy5.5-CD45RO (BioLegend, UCHL1, catalog no. 304222, RRID: AB_2174124), BUV395-CD3 (BD Biosciences, UCHT1, catalog no. 563548, RRID: AB_2744387), APC-FOXP3 (Thermo Fisher Scientific, PCH101, catalog no. 17–4776–42, RRID: AB_1603280), FITC-Ki67 (BD, B56, catalog no. 556026, RRID: AB_396302). T cells activation with phorbol-12-myristate 13-acetate/ionomycin (PMA/iono) was performed according to the manufacturer's protocol (BioLegend, catalog no. 423301).

Spleen flow cytometry

Spleen single cell suspensions were prepared using methods described previously (25). Splenocytes were stained with BV711-CD4 (BioLegend, SK3, catalog no. 344648, RRID: AB_2734350), BUV395-CD3 (BD Biosciences, UCHT1, catalog no. 563548, RRID: AB_2744387), and 7-AAD viability staining solution (eBiosciences, catalog no. 00–6993–50).

Whole brain flow cytometry

Following dissection, whole brains were mechanically homogenized and passed through a 100-μM sterile filter. Cells were treated with a CNS-Specific Percoll Isotonic solution (Percoll – Cytiva) to remove myelin. Brain cells were stained with BV421-CD4 (BioLegend, OKT4, catalog no. 304222, RRID: AB_2562134), PE/Cy7-CD25 (BioLegend, M-A251, catalog no. 356108, RRID: AB_2561975), PE-CD45RA (BioLegend, HI100, catalog no. 304108, RRID: AB_314412), PerCP/Cy5.5-CD45RO (BioLegend, UCHL1, catalog no. 304222, RRID: AB_2174124), BUV395-CD3 (BD Biosciences, UCHT1, catalog no. 563548, RRID: AB_2744387), APC-FOXP3 (Thermo Fisher Scientific, PCH101, catalog no. 17–4776–42, RRID: AB_1603280), and LIVE/DEAD Fixable Green Dead Cell Stain Kit (Thermo Fisher Scientific, catalog no. L23101P).

Biodistribution study

Mice were administered [^{64}Cu]Cu-NOTA-IAB41 via tail vein and scarified at indicated time points by CO_2 asphyxiation. Organs were collected and levels of radioactivity for each organ were measured using a PerkinElmer γ-counter. Normalized tracer uptake, which is expressed by percentage of injected dose per gram of body weight (%ID/g), was calculated as the amount of radioactivity divided by the organ mass and decay-corrected injected dose using mass standards of [^{64}Cu]Cu-NOTA-IAB41 injectate.

FACS

$CD4^+$ cells were isolated from bulk PBMCs using the $CD4^+$ T-Cell Isolation Kit with MicroBeads for column-based magnetic-activated cell sorting (MACS; Miltenyi Biotech, catalog no. 130–096–533). MACS was performed according to the manufacturers protocol. Cells were stained with PE/Cy7-CD25 (BioLegend, M-A251, catalog no. 356108, RRID: AB_2561975), PE-CD45RA (BioLegend, HI100, catalog no. 304108, RRID: AB_314412), PerCP/Cy5.5-CD45RO (BioLegend, UCHL1, catalog no. 304222, RRID: AB_2174124), BUV395-CD3 (BD Biosciences, UCHT1, catalog no. 563548, RRID: AB_2744387), and LIVE/DEAD Green Dead Cell Stain Kit (Thermo Fisher Scientific, catalog no. L23101). Pooled cells from all groups were used to generate the LIVE/DEAD single-color control, all fluorescence minus one (FMO) controls, and unstained controls. Ultracomp eBeads (Thermo Fisher Scientific, catalog no. 01–2222–41) were stained to generate single color controls. Analysis was performed using FlowJo (Version 10, RRID: SCR_008520). FACs gating strategy is detailed in Supplementary Fig. S1.

PET and CT imaging

PET and CT imaging and image quantification were conducted using methods described previously (25). Mice received MRI scans 2 to 3 days prior to PET/CT imaging. We quantified the %ID/g in the tumor. Tumor region of interest (ROI) was determined by MRI. The ROI size for nontumor bearing mice in the striatum was determined by the average tumor size in the tumor-bearing cohort (17.5 mm^3). ROI placement was guided by the MRI for tumor-bearing mice.

MRI

MRI imaging was conducted using methods described previously (25).

Autoradiography

Following transcardial perfusion with PBS 24 hours after injection of [^{64}Cu]Cu-NOTA-IAB41, mouse brains were embedded in optimal cutting temperature (OCT) compound Slides with 3 × 10 μmol/L striatal (tumor-containing) sections were captured IHC. Slides with 3 × 40 μmol/L striatal (tumor-containing), hippocampal, and cerebellar sections were taken for autoradiography and subsequent hematoxylin and eosin (H&E) staining. The 3 × 40 μmol/L slides were exposed to the autoradiography film for 10 half-lives. The film was scanned using a Typhoon phosphoimager. FIJI (version 2.0, RRID: SCR_002285) was used to visualize the autoradiography images.

IHC

IHC was performed using 5-μmol/L-thick coronal sections of striatum from formalin-fixed, paraffin-embedded mouse brain tissue. Sections were stained using the Ventana Bench-mark ULTRA IHC automated staining system (Ventana Medical Systems, Roche-AstraZeneca). Immune cells were visualized using anti-human-CD4 (Abcam, EPR6855, ab133616, RRID: AB_2819211, 170 μg/mL). IHC was imaged using HALO software (version 3.0.311.228, Indica Lab). For OCT-embedded sections, the detection of human-CD4 by IHC was performed at Molecular Cytology Core Facility, Memorial Sloan Kettering Cancer Center using Discovery XT Processor (Ventana Medical Systems, Roche-Astra-Zeneca). The anti-human-CD4 antibody (Ventana-Roche, catalog no. 790–4423) was used in 1:5 prediluted concentration. slides were

counterstained with hematoxylin and coverslipped with Permount (Thermo Fisher Scientific).

Statistical analysis

Statistical analyses were performed using GraphPad Prism (version 8). All data presented were analyzed using unpaired, two-tailed Student *t* tests and differences >95% confidence level were considered significant.

Data availability

The data generated in this study are available within the article and its Supplementary Data files.

Results

[^{64}Cu]Cu-NOTA-IAB41 synthesis and radiolabeling

The anti-CD4 minibody IAB41 consists of two scFv regions bound to a truncated Fc region (CH3 domain-alone). The small size of the minibody (~80 kDa) enables a shorter circulation half-life relative to full length antibodies (27). We radiolabeled the minibody with ^{64}Cu, a positron emitter whose half-life (12.7 hours) is well matched to that of the minibody. The IAB41 minibody was incubated with an 80-fold excess of *p*-SCN-Bn-NOTA chelator in metal-free PBS to generate NOTA-IAB41. NOTA-IAB41 was subsequently incubated with ^{64}Cu at pH 5.5 in 250 mmol/L metal-free ammonium acetate and purified with >99% radiochemical purity quantified by instant thin layer chromatography (iTLC; **Fig. 1A** and **B**). We also evaluated the stability of [^{64}Cu]Cu-NOTA-IAB41 in human serum by iTLC and found [^{64}Cu]Cu-NOTA-IAB41 maintained its stability at 4, 24, and 48 hours (**Fig. 1C**).

To ensure NOTA-IAB41 maintained its capacity to bind human CD4, we performed an immunoreactivity assay. The immunoreactive fraction (%Target Binding Fraction = [Counts per Minute (CPM)$_{Beads}$]/[CPM$_{Beads}$ + CPM$_{Supernatent}$ + CPM$_{Wash1}$ + CPM$_{Wash2}$]) of [^{64}Cu]Cu-NOTA-IAB41 was 70.7% (±1.4 SD, $n = 3$). Further, the target binding fraction was significantly higher than the non-CD4 containing control (0.8%, ±0.3 SD, $n = 3$, $P < 0.0001$) and was outcompeted by a 100-fold excess of unlabeled NOTA-IAB41 demonstrating CD4 specificity (17.9%, ±3.3 SD, $n = 3$, $P < 0.0001$, **Fig. 1D**).

The CD4-targeted minibody detects all CD4$^+$ T-cell subsets

CD4$^+$ T cells can be categorized into three phenotypic states which perform distinct functions (**Fig. 2A**). Naïve CD4$^+$ T cells have not yet encountered their cognate antigen. Upon antigen encounter, CD4$^+$ T cells become activated and differentiate into functionally distinct CD4 T-cell subsets; conventional CD4$^+$ T cells (which include the T_H subtypes), referred to as "activated" or CD4$^+$ T_{regs} (6, 28). T_{regs} are functionally distinct from conventional CD4$^+$ T cells and are associated with immunosuppression (12).

Because all CD4$^+$ T-cell subtypes (naïve, activated conventional T_H, and T_{regs}) have been observed in the context of tumors, we evaluated the ability of [^{64}Cu]Cu-NOTA-AB41 to detect these distinct CD4 T-cell populations (6). We sorted CD4$^+$ cells from bulk PBMCs (PBMC Donor 1, Supplementary Table S1) by MicroBeads for column-based magnetic cell isolation (MAC;

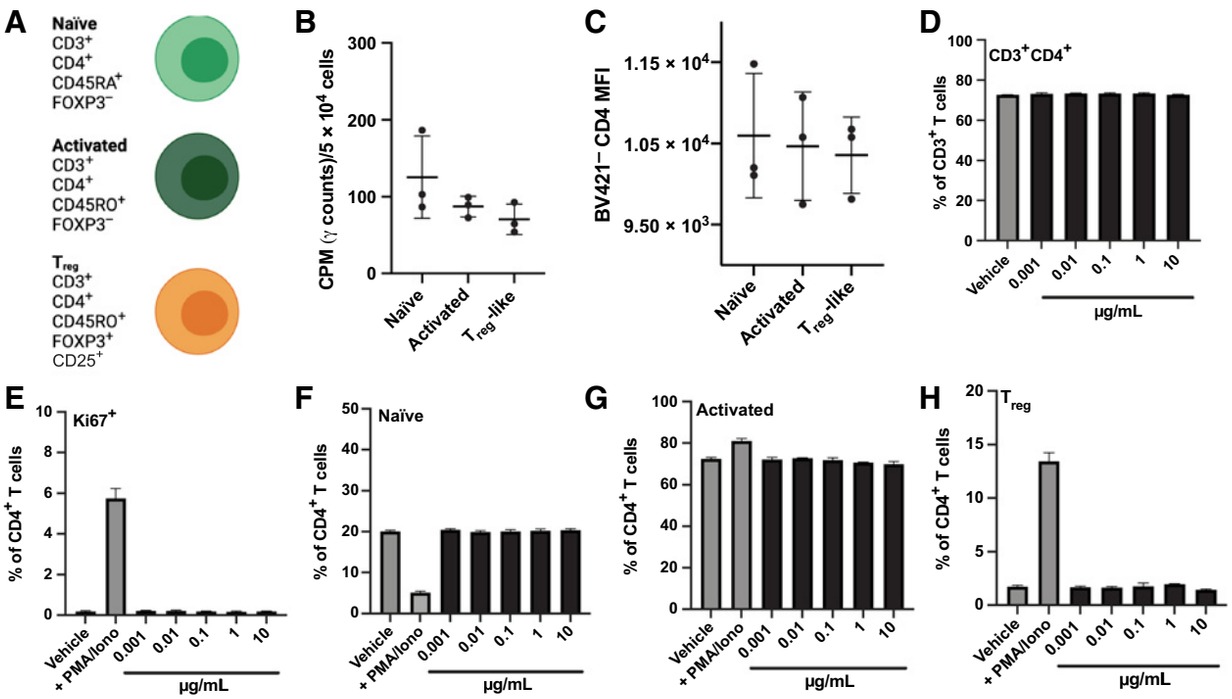

Figure 2.

[^{64}Cu]Cu-NOTA-IAB41 detects CD4$^+$ T-cell subtypes, but neither depletes nor activates CD4$^+$ T cells *in vitro*. **A,** Schematic depicting CD4$^+$ T-cell subtypes analyzed. **B,** [^{64}Cu]Cu-NOTA-IAB41 bound FACS sorted CD4$^+$ T-cell subtypes, quantified by γ-counting. **C,** Bulk PBMC flow cytometry quantifying the MFI for 3 CD4$^+$ T-cell subtypes. Dose-dependent effect of NOTA-IAB41 on (**D**) proportion of CD4$^+$ T cells (**E**) Ki67 expression (**F**) proportion of naïve CD4$^+$ T cells (**G**) proportion of activated conventional CD4$^+$ T cells (**H**) and CD4$^+$ regulatory T cells measured by flow cytometry. For all panels error bars are the SD.

Miltenyi Biotech). We then performed FACS for $CD3^+CD45RA^+$-$CD45RO^-$ (naïve), $CD3^+CD45RA^-CD45RO^+CD25^-$ (activated), or $CD3^+CD45RA^-CD45RO^+CD25^+$ (T_{reg}-like) cells (gating strategy found in Supplementary Fig. S1). We found that [^{64}Cu]Cu-NOTA-IAB41 was able to detect all $CD4^+$ T-cell subtypes (**Fig. 2B**).

We next performed flow cytometry on bulk PBMCs from the same donor to determine the relative expression of CD4 on each T-cell subtype quantified by mean fluorescence intensity (MFI; PBMC Donor 1, Supplementary Table S1). We found that naïve ($CD3^+CD45RA^+CD45RO^-$, MFI = 10,597.6, ± 766.3 SD, n = 3), activated ($CD3^+CD45RA^-CD45RO^+CD25^-$, MFI = 10,466.3, ± 666.5 SD, n = 3) and T_{reg}-like cells ($CD3^+CD45RA^-CD45RO^+CD25^+$, MFI = 10,356 ± 469 SD, n = 3) had no significant difference in MFI, suggesting similar levels of CD4 expression within each cell population (**Fig. 2C**, gating strategy found in Supplementary Fig. S2). This reflects the nonsignificant difference in [^{64}Cu]Cu-NOTA-IAB41 binding across $CD4^+$ T-cell subtypes (**Fig. 2B**), indicating CD4 expression corresponds to the amount of activity bound.

The IAB41 minibody binds human CD4 but does not contain a functional Fc region, presumably rendering IAB41 biologically inert. Freise and colleagues reported that a mouse CD4-targeted cys-diabody (lacking an Fc region) was non-depleting in vivo, but did show effects on proliferation and T cell biology at higher doses, which could be avoided by limiting the amount of protein administered (19). To determine whether NOTA-IAB41 impacted the depletion, proliferation, or activation of $CD4^+$ T cells, we assessed the dose–response of NOTA-IAB41-treated PBMCs ranging from 0.001 to 10 μg/mL for 48 hours (flow cytometry panel validation can be found in Supplementary Fig. S3). We found that the proportion of $CD4^+$ T cells was constant across treatment groups, demonstrating that NOTA-IAB41 does not deplete $CD4^+$ T cells *in vitro* (**Fig. 2D**, $CD3^+CD4^+/CD3^+$). Further, NOTA-IAB41 does not alter the expression of the proliferation marker Ki67 on $CD4^+$ T cells relative to vehicle control (**Fig. 2E**, $CD3^+CD4^+Ki67^+/CD3^+CD4^+$). Phorobol myistate/ionomycine treatment (PMA/iono) treatment induces nonspecific T-cell activation and proliferation and was used as a positive control for flow cytometry. In addition, NOTA-IAB41 does not alter the proportion of naïve ($CD3^+CD4^+$ $FOXP3^-CD45RA^+CD45RO^-/CD3^+CD4^+$), activated conventional ($CD3^+CD4^+FOXP3^-CD45RA^-CD45RO^+/CD3^+CD4^+$) $CD4^+$ T cells, or T_{regs} ($CD3^+CD4^+FOXP3^+CD25^+/CD3^+CD4^+$), relative to the vehicle control (**Fig. 2F**–H, gating strategy can be found in Supplementary Fig. S4).

We subsequently repeated this assay with a second PBMC donor and found similar results (Supplementary Fig. S5, PBMC Donor 2, Supplementary Table S1). After determining that NOTA-IAB41 does not appear to alter $CD4^+$ T-cell persistence, proliferation, or activation *in vitro*, we assessed the minibody's ability to image human $CD4^+$ T cells *in vivo*.

[^{64}Cu]Cu-NOTA-IAB41 detects human $CD4^+$ T cells *in vivo*

To evaluate the ability of [^{64}Cu]Cu-NOTA-IAB41 to visualize human $CD4^+$ T cells, we generated a PBMC HIS mouse model. NOD.Cg-*Prkdc*^{scid} Il2rg^{tm1Sug}/JicTac (CIEA NOG) mice were either intravenously injected with human PBMCs from a single donor (+ PBMCs) or a vehicle control (−PBMCs) and 3 weeks following, both groups were injected with [^{64}Cu]Cu-NOTA-IAB41 (PBMC Donor 3, Supplementary Table S1). Representative PET/CT images of + PBMC mice demonstrate uptake in the spleen, lung, liver, and kidney (**Fig. 3A**). Organs of interest were extracted following PET/CT imaging and the % injected dose (ID) per gram of tissue was

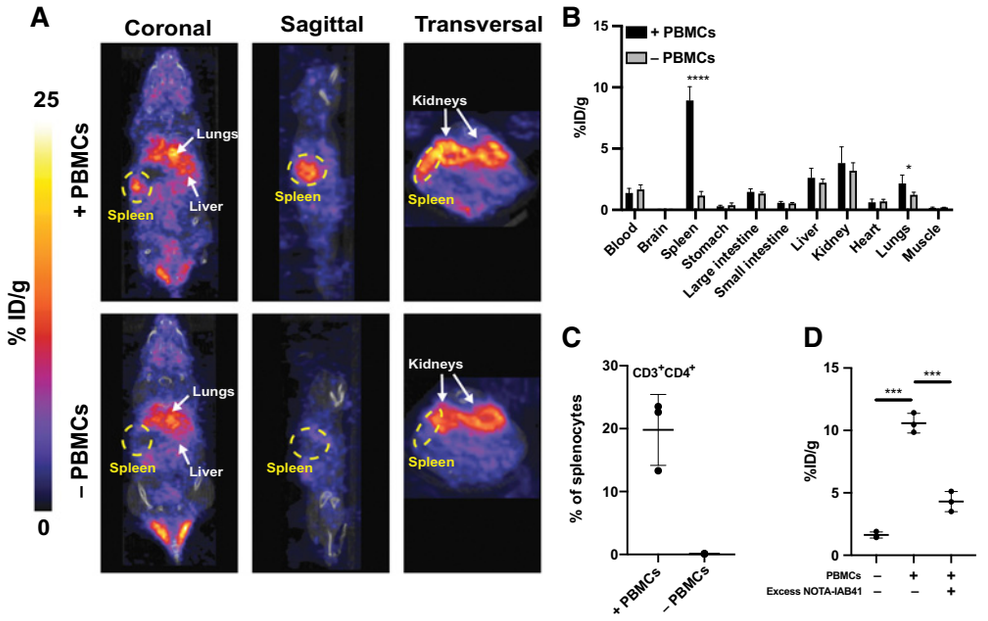

Figure 3.
[^{64}Cu]Cu-NOTA-IAB41 PET imaging of humanized nontumor bearing mice. **A,** Representative PET/CT images of + PBMC and − PBMC CIEA NOG mice 4 hours following [^{64}Cu]Cu-NOTA-IAB41 tracer injection (n = 4/condition). **B,** *Ex vivo* biodistribution of [^{64}Cu]Cu-NOTA-IAB41 in humanized and nonhumanized CIEA NOG mice 24 hours after tracer injection quantified by gamma counting (n = 4/condition). **C,** Quantification of splenic $CD3^+CD4^+$ T cells 3 weeks following humanization in + and − PBMC CIEA NOG mice. **D,** Splenic uptake of [^{64}Cu]Cu-NOTA-IAB41 or [^{64}Cu]Cu-NOTA-IAB41 plus 5-fold excess cold NOTA-IAB41 3 weeks following humanization in + PBMC and − PBMC mice. For all panels, *, $P \le 0.05$; ***, $P \le 0.001$; ****, $P \le 0.0001$. Error bars are the SD.

quantified by *ex vivo* gamma counting. The uptake in + PBMC spleens (8.9% ID/g ± 1.1 SD, $n = 4$, $P < 0.0001$) and lungs (2.2% ID/g, 0.7 ± SD, $n = 4$, $P = 0.0450$) was significantly higher than - PBMCs controls (**Fig. 3B**). Splenic and lung $CD4^+$ T-cell infiltrates have been previously reported in PBMC HIS mouse models as the mice develop graft-versus-host disease (29).

To determine whether [^{64}Cu]Cu-NOTA-IAB41 uptake in the spleen is a result of the presence of human $CD4^+$ T cells, we extracted the spleen of + PBMC mice 3 weeks following humanization and found that 19.8% ($CD3^+CD4^+$/total cells) of splenocytes were $CD4^+$ T cells (±5.6 SD, $n = 3$, **Fig. 3C**, gating strategy can be found in Supplementary Fig. S6). To determine whether [^{64}Cu]Cu-NOTA-IAB41 uptake in the lung represents organ infiltration by human $CD4^+$ cells, we extracted the lungs of + PBMC and − PBMC mice 3 weeks post-humanization and performed IHC human CD4. $CD4^+$ cells were present in the lung of + PBMC mice and absent in the lungs of − PBMC mice ($n = 3$, Supplementary Fig. S7). We next evaluated whether [^{64}Cu]Cu-NOTA-IAB41 is specific to human CD4+ T cells *in vivo* we assessed whether a 5-fold excess of unlabeled NOTA-IAB41 would be sufficient to block [^{64}Cu]Cu-NOTA-IAB41. Three weeks following PBMC injection, + PBMC mice were injected with [^{64}Cu]Cu-NOTA-IAB41-alone or [^{64}Cu]Cu-NOTA-IAB41 + a 5-fold excess of unlabeled NOTA-IAB41. We also included a − PBMC control. We found that excess unlabeled NOTA-IAB41 was sufficient to significantly reduce the PET signal of [^{64}Cu]Cu-NOTA-IAB41 in the spleen (+PBMCs 11.3%ID/g, ±0.7 SD, $n = 3$; + PBMCs + excess unlabeled NOTA-CD4 4.9% ID/g, ±1.0 SD, $n = 3$, $P = 0.001$), suggesting specificity of the tracer (**Fig. 3D**, PBMC Donor 4, Supplementary Table S1). The PET signal in the spleen of the + PBMC group was modestly higher than that of the prior imaging experiment (**Fig. 3B**). This is likely due to differences in splenic T-cell burden as these two experiments were performed with distinct PBMC donors (25).

[^{64}Cu]Cu-NOTA-IAB41 images $CD4^+$ brain TILs

PET/CT images and *ex vivo* gamma counting demonstrated no uptake of [^{64}Cu]Cu-NOTA-IAB41 in non-diseased brain, suggesting low background suitable for use of [^{64}Cu]Cu-NOTA-IAB41 for neuroimaging (**Fig. 3B**). Our group has previously found that the CD8-targeted minibody IAB22M2C (ImaginAb) readily images CD8+ TILs in orthotopically transplanted GBM tumors in the brain (25). To determine whether the minibody-based PET probe [^{64}Cu]Cu-NOTA-IAB41 images CD4+ TILs in a humanized brain tumor model, we first evaluated whether the implantation of an orthotopic GBM was sufficient to induce the infiltration of human CD4+ T cells to the TME. To do so, we intracranially injected a GBM PDX into CIEA NOG mice and three weeks later we humanized the mice (+PBMCs) from a partial-HLA matched donor (workflow **Fig. 4A**). Patient-derived orthotopic GBM xenograft models recapitulate the molecular and histopathological features of GBM, including heterogeneous blood brain barrier permeability, and hence represent a suitable model system to evaluate radiotracer uptake (30, 31). We found human CD4+ T cells infiltrate into the GBM 3 weeks following humanization by IHC (**Fig. 4B**, PDX 160721–1, PBMC Donor 3, Supplementary Table S1). We next determined the proportion of CD4+ T cell subtypes in the brain TME by flow cytometric analysis. Humanized GBM PDX 160721–1-bearing mice were prepared according to the workflow in **Fig. 3A**. Whole brains were extracted for flow cytometry (gating strategy found in Supplementary Fig. S8). The majority of CD4+ T cells in the brain were either T_{regs} ($CD3+CD4+FOXP3+CD25+$ cells/$CD3+CD4+$ cells, 19.1% ± 13.0 SD, $n = 6$) or activated conventional CD4+ T cells ($CD3+CD4+FOXP3-CD45RA-CD45RO+$ cells/$CD3+CD4+$ cells, 55.1%, ± 12.5 SD, $n = 6$) with a minority of naïve CD4+ T cells ($CD3+CD4+FOXP3-CD45RA+CD45RO-$/$CD3+CD4+$ cells, 3.1%, ±1.3 SD, $n = 6$) (**Fig. 4C**, PBMC Donor 5, Supplementary Table S1). The ratio of activated conventional CD4+ T cells to T_{regs} is the inverse of reports in GBM patients. This disparity is likely due to the PBMC mouse models development of graft-versus-host disease (32, 33). However, these cell types are key in anti-tumor immunity and their presence in the brain TME of the GBM HIS mouse model enables the evaluation of their detection *in vivo*.

We next sought to determine whether [^{64}Cu]Cu-NOTA-IAB41 images CD4+ TILs in the brain. To do so we implanted CIEA NOG mice with PDX 160721–1 (+Tumor) and subsequently humanized with PBMCs (+PBMCs) (PBMC Donor 3, Supplementary Table S1). We also generated tumor-bearing non-humanized (+Tumor − PBMCs) and non-tumor-bearing humanized (−Tumor + PBMCs) controls. Non-tumor-bearing controls received a sham intracranial injection. We observed the highest signal in the tumor-bearing humanized (+Tumor + PBMCs) brain 24 hours following radiotracer injection with relatively little uptake in the non-tumor bearing and non-humanized controls (representative PET/CT images, **Fig. 4D**). Mean uptake in + Tumor + PBMC mice was 1.6% ID/g (± 0.5 SD, $n = 3$) which was significantly higher than + Tumor − PBMC mice (0.6% ID/g, ± 0.1 SD, $n = 4$, $P = 0.0086$) and - Tumor + PBMC mice (0.6% ID/g, ± 0.1 SD, $n = 3$, $P = 0.0220$, **Fig. 4E**). We repeated this workflow with a second GBM PDX 160615–1 and again found significantly higher uptake in the + Tumor + PBMC group (1.8% ID/g, ± 0.5 SD, $n = 4$) relative to the + Tumor − PBMCs (0.7% ID/g, ± 0.2 SD, $P = 0.0040$) and the - Tumor + PBMCs groups (0.3% ID/g, ± 0.06 SD, $n = 3$, $P = 0.0169$, **Fig. 4F**; representative images of PDX 160615–1 can be found in Supplementary Fig. S9, PBMC Donor 4, Supplementary Table S1).

To determine whether [^{64}Cu]Cu-NOTA-IAB41 uptake is specific to brain parenchymal CD4+ TILs, we performed autoradiography and IHC. Following PET/CT imaging of PDX 160721–1 and PDX 160615–1, mice were perfused to clear the blood-pool from the brain and whole brain was embedded in OCT compound. We acquired 40 μmol/L sections for autoradiography and H&E. In addition, we took 10 μmol/L serial sections for anti-human-CD4 IHC. We found that tracer uptake localizes to CD4+ T cell infiltrate in the brain of + Tumor + PBMC mice with little uptake in + Tumor - PBMC controls (PDX 160721–1, **Fig. 4G**; PDX 160615–1, Supplementary Fig. S10). Additionally, we acquired striatal (tumor-bearing), hippocampal, and cerebellar sections and found that tracer uptake localizes to tumor bearing, CD4+ T cell infiltrated brain sections (PDX 160615–1, **Fig. 4H**). These results corroborate our previous findings by PET, indicating [^{64}Cu]Cu-NOTA-IAB41 uptake is specific to human CD4+ T cell infiltrate.

Discussion

$CD4^+$ T cells play an integral role in driving antitumor immunity and there is growing evidence suggesting the role of $CD4^+$ T cells in brain tumor immune evasion. Immunosuppressive $CD4^+$ T cells are found within the GBM TME whereas conventional $CD4^+$ subsets are deprived from the TME (34). Higher grade gliomas are associated with increased T_{reg} infiltrate (35). Further, depletion of T_{regs} in the SMA-560 mouse glioma model resulted in enhanced tumor rejection and improved survival (36). However, conclusions have been limited

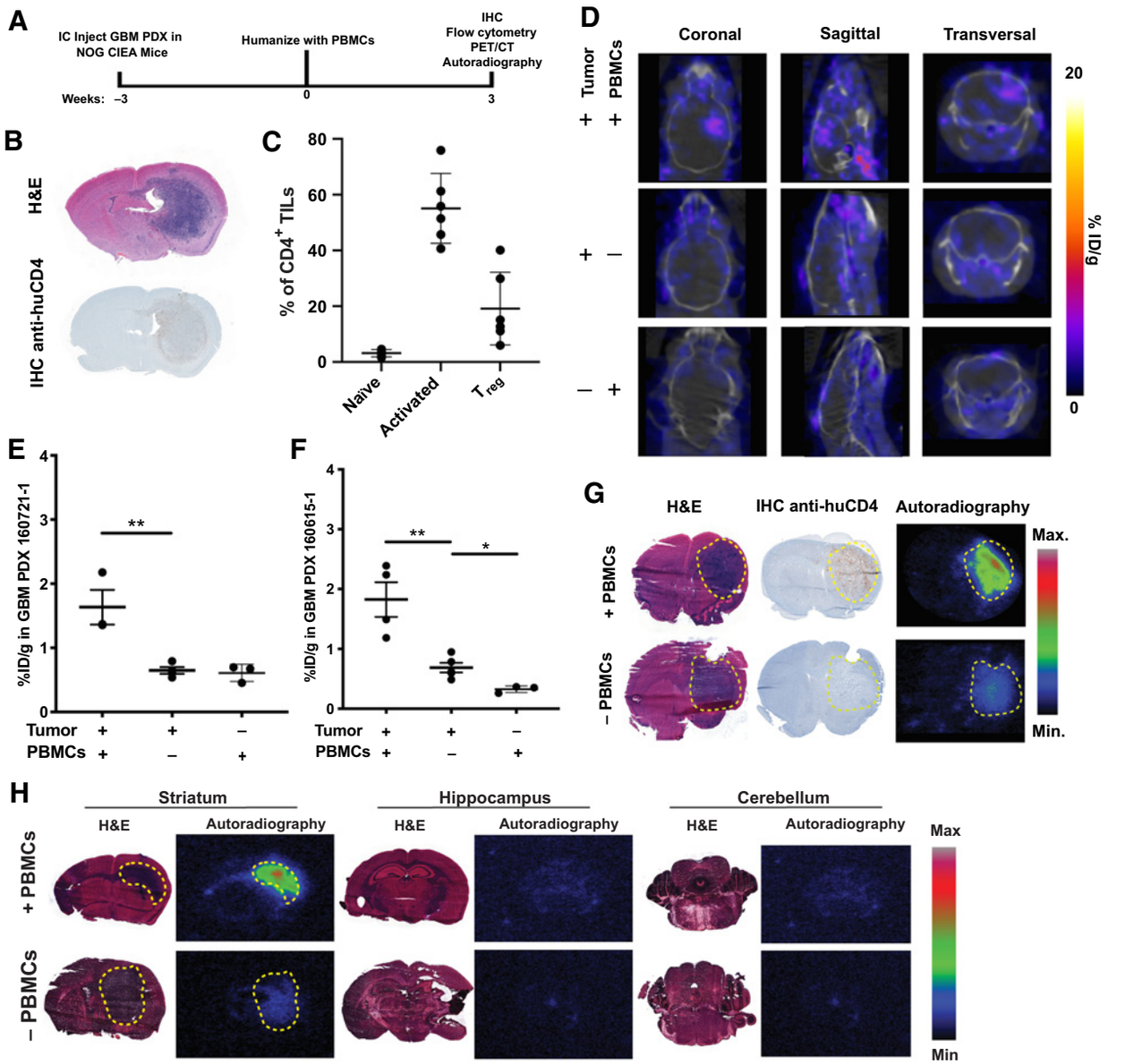

Figure 4.

[^{64}Cu]Cu-NOTA-IAB41 images CD4$^+$ TILs in two humanized mouse models of GBM. **A,** Experimental timeline highlighting the order of orthotopic PDX engraftment, humanization with HLA donor matched PBMCs, imaging, and necropsy (top). **B,** Visualization of tumor and CD4$^+$ T-cell infiltrate by H&E (top) and IHC (bottom; $n = 3$). **C,** Quantification of whole brain flow cytometry reflecting the proportion of three CD4$^+$ TIL subtypes in the humanized GBM PDX 160721–1, PBMC donor 4 ($n = 6$). **D,** Co-registered PET/CT images of + Tumor + PBMC (top), + Tumor − PBMC (middle), and − Tumor + PBMC (bottom) mice 24 hours following [^{64}Cu]Cu-NOTA-IAB41 tracer injection. −Tumor mice received a sham IC injection. ($n = 4$/condition). **E** and **F,** Quantification of tracer uptake for PDX model 160721–1 donor 4 (**E**) and PDX 160615–1, PBMC donor 5 (**F**). **G,** H&E staining, IHC for human CD4, and autoradiography ($n = 3$/condition) of PDX 160721–1. Sections were acquired 24 hours after injection with radiotracer. **H,** Distribution of [^{64}Cu]Cu-NOTA-IAB41 in PDX 160615–1-bearing mouse brains. H&E and autoradiography ($n = 3$/condition) of PDX 160615–1 (*, $P \le 0.05$; **, $P \le 0.01$). Error bars are the SD.

by a lack of tools to noninvasively monitor CD4$^+$ T-cell kinetics in patients with GBM throughout disease progression and treatment.

Our data demonstrate the capability of [^{64}Cu]Cu-NOTA-IAB41 as a noninvasive imaging agent for human CD4$^+$ T cells in brain tumors.

GBMs are thought to have low cytotoxic CD8$^+$ T-cell infiltrate and relatively high proportions of immunosuppressive T_{regs}, suggesting the applicability of noninvasive CD4-targeted imaging. In contrast to GBMs seen in the clinic, the density of CD4$^+$ TILs seen in our PBMC humanized GBM model system reaches the upper limit of CD4$^+$ T cells visualized by biopsy and there is a higher proportion of activated conventional CD4$^+$ T cells relative to T_{regs} (37). This may be attributed to the inflammatory nature of the PBMC HIS mouse model or PBMC donor-tumor alloreactivity due to mismatch in minor HLA-loci (29). These limitations mitigate drawing conclusions regarding GBM

immuno-biology. However, this model system is an excellent resource to evaluate the capacity of a CD4-targeted PET tracer to detect $CD4^+$ T cells and their subtypes in a brain tumor and in peripheral organs. We were able to determine, using this model system, that [^{64}Cu]Cu-NOTA-IAB41 detects $CD4^+$ T cells both in peripheral organs and in brain tumors and CD4 T cells of distinct lineages and activation states revealing its wide applicability for the detection of $CD4^+$ T cells in various tissues in homeostasis and disease.

The application of noninvasive monitoring of $CD4^+$ T cells in the brain spans beyond cancer. $CD4^+$ T cells have been implicated in a number of autoimmune diseases including those with neuroinflammatory pathology. $CD4^+$ T cells mitigate disease progression in experimental models of multiple sclerosis, a central nervous system autoimmune disorder (38). $CD4^+$ T-cell infiltrate into the brain parenchyma has also been implicated in the pathogenesis of neurodegenerative diseases Parkinson and Alzheimer (39–41). In addition to imaging $CD4^+$ T cells in the brain. CD4-targeted immunoPET may have applications in peripheral immune disorders. Previous work by Freise and colleagues demonstrates the utility of CD4-targeted ImmunoPET in a mouse model of irritable bowel disorder (17). In addition, the PBMC HIS mice used in our study model the development of graft-versus-host disease over time (29).

[^{64}Cu]Cu-NOTA-IAB41 detects human $CD4^+$ T cells regardless of their activation and functional states—including naïve, activated conventional $CD4^+$ T cells, and $T_{regs.}$ [^{64}Cu]Cu-NOTA-IAB41 is also able to detect $CD4^+$ TILs in orthotopic GBM PBMC HIS mouse models. Our PET tracer does not differentiate between $CD4^+$ T-cell subtypes, a potential limitation since $CD4^+$ T-cell subtypes play distinct roles in antitumor immune response and resistance (6). At the current time, however, the role of specific $CD4^+$ T-cell subsets in GBM antitumor response remains to be defined and our current strategy hence represents an inclusive first approach to quantify all $CD4^+$ T-cell *in vivo*. This could be particularly informative when used in conjugation with radiotracers directed against other immune cells, for example $CD8^+$ T cells (25). As the technology of multiplexed PET evolves, one can envision the use of multiple tracers in-tandem to delineate cell subtypes without the need of biopsy (42). An additional limitation is the observed uptake of [^{64}Cu]Cu-NOTA-IAB41 in the liver and kidney of − PBMC mice and this signal likely represents nonspecific uptake (2–4% ID/g) of [^{64}Cu]Cu-NOTA-IAB41. This nonspecific uptake in the kidney and the liver is likely a result of excretion of the radiotracer, a limitation that may limit the utility of the tracer to image $CD4^+$ T-cell infiltration in these particular organs (25, 27).

The anti-CD4 minibody IAB41 detects human $CD4^+$ T cells without depleting or altering proliferation or phenotype. Further, [^{64}Cu]Cu-NOTA-IAB41 images $CD4^+$ TILs in orthotopic PBMC HIS mouse models of GBM. The clinical capacity of IAB41 immunoPET should be further investigated.

Authors' Disclosures

I.K. Mellinghoff reports grants from NINDS, NIH, Emerson Collective, and National Brain Tumor Society during the conduct of the study; and reports serving as a consultant for Agios Pharmaceuticals, Inc., Black Diamond Therapeutics, Debiopharm Group, Puma Biotechnology, Servier Pharmaceuticals, Voyager Therapeutics, DC Europa Ltd., Kazia Therapeutics, Novartis, Cardinal Health, Roche, Vigeo Therapeutics, Samus Therapeutics, A NextCure, and research grants from Amgen, Bristol Myers Squibb, Eli Lilly, Erasca, Genentech, General Electric and Kazia Therapeutics. J.S. Lewis reports grants from NIH, National Brain Tumor Society, Emerson Collective Cancer Fund, and other support from ImaginAB during the conduct of the study. No disclosures were reported by the other authors.

Authors' Contributions

V.L. Nagle: Conceptualization, data curation, formal analysis, supervision, funding acquisition, investigation, methodology, writing–original draft, writing–review and editing. **C.J. Hertz:** Formal analysis, investigation, methodology, writing–review and editing. **K.E. Henry:** Resources, data curation, software, supervision, investigation, methodology, writing–review and editing. **M.S. Graham:** Investigation, methodology, writing–review and editing. **C. Campos:** Resources, validation, investigation. **N. Pillarsetty:** Supervision, writing–review and editing. **A. Schietinger:** Conceptualization, supervision, writing–review and editing. **I.K. Mellinghoff:** Conceptualization, supervision, funding acquisition, writing–review and editing. **J.S. Lewis:** Conceptualization, supervision, funding acquisition, writing–review and editing.

Acknowledgments

We gratefully acknowledge the Molecular Cytology, Flow Cytometry, Radiochemistry and Molecular Imaging Probes Core, and the Small Animal Imaging Cores at MSK supported by NIH grant no. P30 CA08748. The anti-human minibody (IAB41) was a generous gift from ImaginAb Inc. This study was supported by NIH NINDS R35 NS105109-01 (to I.K. Mellinghoff), NCI R35 CA232130 (to J.S. Lewis), NIH T32 GM73546 (to V.L. Nagle), the National Brain Tumor Society Defeat GBM initiative (to I.K. Mellinghoff), and the Emerson Collective Cancer Fund (to I.K. Mellinghoff, J.S. Lewis, A. Schietinger). **Figure 2A** was made in Biorender.com.

The costs of publication of this article were defrayed in part by the payment of page charges. This article must therefore be hereby marked *advertisement* in accordance with 18 U.S.C. Section 1734 solely to indicate this fact.

Received November 3, 2021; revised January 3, 2022; accepted February 2, 2022; published first February 7, 2022.

References

1. Drake CG, Lipson EJ, Brahmer JR. Breathing new life into immunotherapy: review of melanoma, lung and kidney cancer. Nat Rev Clin Oncol 2014;11:24–37.
2. Tawbi HA, Forsyth PA, Algazi A, Hamid O, Hodi FS, Moschos SJ, et al. Combined Nivolumab and Ipilimumab in melanoma metastatic to the brain. N Engl J Med 2018;379:722–30.
3. Goldberg SB, Schalper KA, Gettinger SN, Mahajan A, Herbst RS, Chiang AC, et al. Pembrolizumab for management of patients with NSCLC and brain metastases: long-term results and biomarker analysis from a non-randomised, open-label, phase 2 trial. Lancet Oncol 2020;21:655–63.
4. Jackson CM, Choi J, Lim M. Mechanisms of immunotherapy resistance: lessons from glioblastoma. Nat Immunol 2019;20:1100–9.
5. Chen DS, Mellman I. Oncology meets immunology: the cancer-immunity cycle. Immunity 2013;39:1–10.
6. Tay RE, Richardson EK, Toh HC. Revisiting the role of CD4(+) T cells in cancer immunotherapy-new insights into old paradigms. Cancer Gene Ther 2021;28:5–17.
7. Antony PA, Piccirillo CA, Akpinarli A, Finkelstein SE, Speiss PJ, Surman DR, et al. CD8+ T cell immunity against a tumor/self-antigen is augmented by CD4+ T helper cells and hindered by naturally occurring T regulatory cells. J Immunol 2005;174:2591–601.
8. Berner V, Liu H, Zhou Q, Alderson KL, Sun K, Weiss JM, et al. IFN-gamma mediates CD4+ T-cell loss and impairs secondary antitumor responses after successful initial immunotherapy. Nat Med 2007;13:354–60.
9. Rittig SM, Haentschel M, Weimer KJ, Heine A, Muller MR, Brugger W, et al. Intradermal vaccinations with RNA coding for TAA generate CD8+ and CD4+ immune responses and induce clinical benefit in vaccinated patients. Mol Ther 2011;19:990–9.
10. Ott PA, Hu Z, Keskin DB, Shukla SA, Sun J, Bozym DJ, et al. An immunogenic personal neoantigen vaccine for patients with melanoma. Nature 2017;547:217–21.
11. Borst J, Ahrends T, Babala N, Melief CJM, Kastenmuller W. CD4(+) T cell help in cancer immunology and immunotherapy. Nat Rev Immunol 2018;18:635–47.

12. Sharabi A, Tsokos MG, Ding Y, Malek TR, Klatzmann D, Tsokos GC. Regulatory T cells in the treatment of disease. Nat Rev Drug Discov 2018;17:823–44.
13. Cloughesy TF, Mochizuki AY, Orpilla JR, Hugo W, Lee AH, Davidson TB, et al. Neoadjuvant anti-PD-1 immunotherapy promotes a survival benefit with intratumoral and systemic immune responses in recurrent glioblastoma. Nat Med 2019;25:477–86.
14. Lim M, Xia Y, Bettegowda C, Weller M. Current state of immunotherapy for glioblastoma. Nat Rev Clin Oncol 2018;15:422–42.
15. Markowitz GJ, Havel LS, Crowley MJ, Ban Y, Lee SB, Thalappillil JS, et al. Immune reprogramming via PD-1 inhibition enhances early-stage lung cancer survival. JCI Insight 2018;3:e96836.
16. Homet Moreno B, Zaretsky JM, Garcia-Diaz A, Tsoi J, Parisi G, Robert L, et al. Response to programmed cell death-1 blockade in a murine melanoma syngeneic model requires costimulation, CD4, and CD8 T cells. Cancer Immunol Res 2016;4:845–57.
17. Freise AC, Zettlitz KA, Salazar FB, Tavare R, Tsai WK, Chatziioannou AF, et al. Immuno-PET in inflammatory bowel disease: imaging CD4-positive T cells in a murine model of colitis. J Nucl Med 2018;59:980–5.
18. Tavare R, McCracken MN, Zettlitz KA, Salazar FB, Olafsen T, Witte ON, et al. Immuno-PET of murine T cell reconstitution postadoptive stem cell transplantation using anti-CD4 and anti-CD8 Cys-diabodies. J Nucl Med 2015;56:1258–64.
19. Freise AC, Zettlitz KA, Salazar FB, Lu X, Tavare R, Wu AM. ImmunoPET imaging of murine CD4(+) T cells using anti-CD4 Cys-diabody: effects of protein dose on T cell function and imaging. Mol Imaging Biol 2017;19:599–609.
20. Kristensen LK, Frohlich C, Christensen C, Melander MC, Poulsen TT, Galler GR, et al. CD4(+) and CD8a(+) PET imaging predicts response to novel PD-1 checkpoint inhibitor: studies of Sym021 in syngeneic mouse cancer models. Theranostics 2019;9:8221–38.
21. Natarajan A, Mayer AT, Reeves RE, Nagamine CM, Gambhir SS. Development of novel ImmunoPET tracers to image human PD-1 checkpoint expression on tumor-infiltrating lymphocytes in a humanized mouse model. Mol Imaging Biol 2017;19:903–14.
22. Zhao H, Wang C, Yang Y, Sun Y, Wei W, Wang C, et al. ImmunoPET imaging of human CD8(+) T cells with novel (68)Ga-labeled nanobody companion diagnostic agents. J Nanobiotechnology 2021;19:42.
23. Griessinger CM, Olafsen T, Mascioni A, Jiang ZK, Zamilpa C, Jia F, et al. The PET-tracer 89Zr-Df-IAB22M2C enables monitoring of intratumoral CD8 T cell infiltrates in tumor-bearing humanized mice after T cell bispecific antibody treatment. Cancer Res 2020;80:2903–13.
24. Wu AM, Pandit-Taskar N. ImmunoPET: harnessing antibodies for imaging immune cells. Mol Imaging Biol 2021.
25. Nagle VL, Henry KE, Hertz CAJ, Graham MS, Campos C, Parada LF, et al. Imaging tumor-infiltrating lymphocytes in brain tumors with [(64)Cu]Cu-NOTA-anti-CD8 PET. Clin Cancer Res 2021;27:1958–66.
26. Sharma SK, Lyashchenko SK, Park HA, Pillarsetty N, Roux Y, Wu J, et al. A rapid bead-based radioligand binding assay for the determination of target-binding fraction and quality control of radiopharmaceuticals. Nucl Med Biol 2019;71:32–8.
27. Tavare R, McCracken MN, Zettlitz KA, Knowles SM, Salazar FB, Olafsen T, et al. Engineered antibody fragments for immuno-PET imaging of endogenous CD8+ T cells in vivo. Proc Natl Acad Sci U S A 2014;111:1108–13.
28. Zhou L, Chong MM, Littman DR. Plasticity of CD4+ T cell lineage differentiation. Immunity 2009;30:646–55.
29. De La Rochere P, Guil-Luna S, Decaudin D, Azar G, Sidhu SS, Piaggio E. Humanized mice for the study of immuno-oncology. Trends Immunol 2018;39:748–63.
30. Vaubel RA, Tian S, Remonde D, Schroeder MA, Mladek AC, Kitange GJ, et al. Genomic and phenotypic characterization of a broad panel of patient-derived xenografts reflects the diversity of glioblastoma. Clin Cancer Res 2020;26:1094–104.
31. Randall EC, Emdal KB, Laramy JK, Kim M, Roos A, Calligaris D, et al. Integrated mapping of pharmacokinetics and pharmacodynamics in a patient-derived xenograft model of glioblastoma. Nat Commun 2018;9:4904.
32. Yamashita K, Choi U, Woltz PC, Foster SF, Sneller MC, Hakim FT, et al. Severe chronic graft-versus-host disease is characterized by a preponderance of CD4(+) effector memory cells relative to central memory cells. Blood 2004;103:3986–8.
33. Ali N, Flutter B, Sanchez Rodriguez R, Sharif-Paghaleh E, Barber LD, Lombardi G, et al. Xenogeneic graft-versus-host-disease in NOD-scid IL-2Rgammanull mice display a T-effector memory phenotype. PLoS One 2012;7:e44219.
34. Dubinski D, Wolfer J, Hasselblatt M, Schneider-Hohendorf T, Bogdahn U, Stummer W, et al. CD4+ T effector memory cell dysfunction is associated with the accumulation of granulocytic myeloid-derived suppressor cells in glioblastoma patients. Neuro Oncol 2016;18:807–18.
35. Heimberger AB, Abou-Ghazal M, Reina-Ortiz C, Yang DS, Sun W, Qiao W, et al. Incidence and prognostic impact of FoxP3+ regulatory T cells in human gliomas. Clin Cancer Res 2008;14:5166–72.
36. Fecci PE, Mitchell DA, Whitesides JF, Xie W, Friedman AH, Archer GE, et al. Increased regulatory T-cell fraction amidst a diminished CD4 compartment explains cellular immune defects in patients with malignant glioma. Cancer Res 2006;66:3294–302.
37. Orrego E, Castaneda CA, Castillo M, Bernabe LA, Casavilca S, Chakravarti A, et al. Distribution of tumor-infiltrating immune cells in glioblastoma. CNS Oncol 2018;7:CNS21.
38. Bailey-Bucktrout SL, Martinez-Llordella M, Zhou X, Anthony B, Rosenthal W, Luche H, et al. Self-antigen-driven activation induces instability of regulatory T cells during an inflammatory autoimmune response. Immunity 2013;39:949–62.
39. Brochard V, Combadiere B, Prigent A, Laouar Y, Perrin A, Beray-Berthat V, et al. Infiltration of CD4+ lymphocytes into the brain contributes to neurodegeneration in a mouse model of Parkinson disease. J Clin Invest 2009;119:182–92.
40. Baruch K, Rosenzweig N, Kertser A, Deczkowska A, Sharif AM, Spinrad A, et al. Breaking immune tolerance by targeting Foxp3(+) regulatory T cells mitigates Alzheimer's disease pathology. Nat Commun 2015;6:7967.
41. Schetters STT, Gomez-Nicola D, Garcia-Vallejo JJ, Van Kooyk Y. Neuroinflammation: microglia and T cells get ready to Tango. Front Immunol 2017;8:1905.
42. Heinzmann K, Carter LM, Lewis JS, Aboagye EO. Multiplexed imaging for diagnosis and therapy. Nat Biomed Eng 2017;1:697–713.